

## AN *HST* LENSING SURVEY OF X-RAY LUMINOUS GALAXY CLUSTERS: I. A 383<sup>1</sup>

GRAHAM P. SMITH,<sup>2,5</sup> JEAN-PAUL KNEIB,<sup>3</sup> HARALD EBELING,<sup>4,6</sup> OLIVER CZOSKE<sup>3,5</sup> & IAN SMAIL<sup>2</sup>

2) Department of Physics, University of Durham, South Road, Durham DH1 3LE, UK

3) Observatoire Midi-Pyrénées, CNRS-UMR5572, 14 Avenue E. Belin, 31400 Toulouse, France

4) Institute for Astronomy, University of Hawaii, 2680 Woodlawn Drive, Honolulu, HI 96822, USA

Received 2000 --; accepted: 2000 --

### ABSTRACT

We present an analysis of the mass distribution in the core of A 383 ( $z = 0.188$ ), one of twelve X-ray luminous galaxy clusters at  $z \sim 0.2$  selected for a comprehensive and unbiased study of the mass distribution in massive galaxy clusters. Deep optical imaging performed by the *Hubble Space Telescope* (*HST*) reveals a wide variety of gravitationally lensed features in the core of A 383, including a giant arc formed from the strongly-lensed images of two background galaxies, two radial arcs in the halo of the central cluster galaxy, several multiply-imaged arcs and numerous arclets. Based upon the constraints from the various lensed features, as well as from color information from ground-based observations, we construct a detailed model of the mass distribution in the central regions of the cluster, taking into account both the cluster-scale potential and perturbations from individual cluster galaxies. Keck spectroscopy of one component of the giant arc identifies it as an image of a star-forming galaxy at  $z = 1.01$  and provides an accurate measurement of the mass of the cluster within the projected radius of the giant arc (65 kpc) of  $(3.5 \pm 0.1) \times 10^{13} M_{\odot}$ . Using the weak shear measured from our *HST* observations we extend our mass model to larger scales and determine a mass of  $(1.8 \pm 0.2) \times 10^{14} M_{\odot}$  within a radius of 250 kpc. On smaller scales we employ the radial arcs as probes of the shape of the mass distribution in the cluster core ( $r \lesssim 20$  kpc), find that the mass profile is more peaked than a single Navarro, Frenk & White (NFW, 1997) profile. Our findings therefore support the proposal that massive cluster cores contain more mass than can be explained by a single cluster-scale NFW profile. The optical and X-ray properties of A 383 indicate the presence of a central cooling flow, for which we derive a mass deposition rate of  $\gtrsim 200 M_{\odot} \text{ yr}^{-1}$ . We also use the X-ray emission from A 383 to obtain independent estimates of the total mass within projected radii of 65 and 250 kpc:  $(4.0^{+1.1}_{-1.7}) \times 10^{13} M_{\odot}$  and  $(1.2 \pm 0.5) \times 10^{14} M_{\odot}$ , which are consistent with the lensing measurements.

*Subject headings:* cosmology: observations — gravitational lensing — clusters of galaxies: individual: A 383 — galaxies: evolution

### 1. INTRODUCTION

Massive clusters of galaxies represent one extreme of the mass spectrum of collapsed structures at the present day. Their properties are expected to reflect predominantly gravitational processes and therefore provide unique insights into the nature and distribution of the dark matter which drives the formation of structure (e.g. Eke et al. 1996; Viana & Liddle 1996; Bahcall, Fan & Cen 1997; Kay & Bower 1999). In particular, accurate measurements of the mass distribution in clusters across a range of scales can be used to test the claim of a universal form for the profiles of dark matter halos (Navarro, Frenk & White 1997, NFW) and hence the nature of dark matter. At large scales the NFW profile falls off as  $\rho \propto r^{-3}$ , steeper than an isothermal model ( $\rho \propto r^{-2}$ ). On smaller scales the NFW profile breaks to a shallower slope with  $\rho \propto r^{-1}$ , whilst retaining a central cusp. Analyses of the mass profiles of dwarf galaxies from dynamical studies have used the apparent lack of a central cusp in the density distribution to reject the form of the NFW profile and argue instead for the existence of self-interacting dark matter (e.g. Moore et al. 1998). However, on larger scales, (e.g. luminous elliptical galaxies and massive clusters of galaxies) the form of the mass profile has yet to be investigated systemati-

cally.

The central regions of massive, compact clusters at moderate redshifts ( $z \lesssim 0.5$ ) act as strong gravitational lenses forming multiple images of serendipitously placed background galaxies (e.g. Smail et al. 1996). The properties of the images of these background galaxies (position, relative surface brightness and parity) can be used to accurately model the distribution of total mass (both baryonic and non-baryonic) within the cluster core (Kneib et al. 1996, K96; Smail et al. 1996; Natarajan et al. 1998). Such mass maps provide the most direct and detailed view of the distribution and morphology of dark matter in the centers of galaxy clusters. Strong gravitational lensing by rich clusters is therefore an ideal observational tool with which to test the halo properties predicted by cosmological models.

The first mass maps constructed from lensing observations were produced in the early and mid-1990's (Tyson et al. 1990; Mellier et al. 1993; Fahlman et al. 1994; Kneib et al. 1994; Smail et al. 1995). A significant improvement arrived with the refurbishment of *HST* which provided the resolution necessary to identify faint, lensed features in the crowded cores of rich clusters (e.g. K96), thereby allowing more detailed mass models to be constructed.

<sup>1</sup>Based on observations with the NASA/ESA *Hubble Space Telescope* obtained at the Space Telescope Science Institute, which is operated by the Association of Universities for Research in Astronomy Inc., under NASA contract NAS 5-26555.

<sup>5</sup>Visiting Astronomer, Canada-France-Hawaii Telescope operated by the National Research Council of Canada, the Centre National de la Recherche Scientifique de France and the University of Hawaii.

<sup>6</sup>Visiting Astronomer at the W.M. Keck Observatory, jointly operated by the California Institute of Technology and the University of California

On small scales, unique constraints can be obtained from radial arcs (rare radially magnified images of background galaxies) which are found in the very centers of a few cluster lenses. Such features are very difficult to detect in ground-based observations, with only a single example known (MS 2137.3–23; Fort et al. 1992; Mellier et al. 1993). In contrast to this, *HST* has uncovered several radial arcs in previously well-studied cluster lenses (e.g. A 370, Smail et al. 1996; AC 114, Natarajan et al. 1998) which enabled the first tests of the form of cluster mass profiles on scales of less than  $\sim 100$  kpc (Williams et al. 1999).

Previous *HST* studies of rich clusters covered a heterogeneous mix of clusters, either selected because they were previously well-studied (e.g. Smail et al. 1997) or because they were known to be strong lenses (e.g. K96; Smail et al. 1996). To study the form of the mass profile in rich clusters in an unbiased fashion we need *HST* observations of an objectively selected cluster sample. Ideally such a sample would be mass-selected; however, in the absence of samples compiled from large-scale weak lensing surveys, X-ray selected cluster samples (Gioia et al. 1990; Ebeling et al. 1998, 2000; DeGrandi et al. 1999; Ebeling, Edge & Henry 2000) are best suited to selecting well-defined samples of massive clusters.

Following this premise, we are conducting a survey of twelve of the most X-ray luminous clusters ( $L_X \geq 8 \times 10^{44}$  erg s $^{-1}$ , 0.1–2.4 keV) in a narrow redshift slice at  $z \sim 0.2$ , selected from the XBACs sample (X-ray Brightest Abell-type Clusters; Ebeling et al. 1996). As XBACs is restricted to Abell clusters (Abell, Corwin & Olowin 1989), it is X-ray flux limited and not truly X-ray selected. However, a comparison with the X-ray selected *ROSAT* Brightest Cluster Sample (BCS, Ebeling et al. 1998, 2000) shows that  $\sim 75\%$  of the BCS clusters in the redshift and X-ray luminosity range of our sample are in fact Abell clusters. Hence, our XBACs sample is, in all practical aspects, indistinguishable from an X-ray selected sample.

In this paper we describe *HST* observations of the core of one of the first clusters observed in our survey, A 383 ( $z = 0.188$ ), which reveal a multitude of strongly-lensed features. In combination with color information obtained from ground-based imaging observations in three passbands, the lensed features are used to produce an accurate model of the mass distribution within the central 500 kpc of the cluster. We complement these results with an analysis of the X-ray properties of A 383 using archival *ROSAT HRI* data. In §2 we describe the observational data, their reduction and analysis, followed in §3 by a discussion of the interpretation of these data and the construction of the lens model of the cluster. Finally in §4 we summarize the main results of our analysis and present our conclusions. We adopt  $H_0 = 50$  kms $^{-1}$  Mpc $^{-1}$  and  $q_0 = 0.5$  throughout. At the cluster redshift  $1'' \equiv 4.0$  kpc in this cosmology.

## 2. DATA REDUCTION AND ANALYSIS

A 383 is a massive cluster of galaxies at  $z = 0.188$  with a core dominated by a luminous cD galaxy (Figs. 1 & 3). The X-ray luminosity from a pointed observation with the *ROSAT HRI* is  $(9.8 \pm 0.3) \times 10^{44}$  erg s $^{-1}$  in the 0.1–2.4 keV band (see §2.4).

### 2.1. HST Imaging

A 383 was observed with the *HST WFPC2* camera on January 25, 2000. Three exposures totaling 7.5 ks were taken through the F702W filter. Each exposure was shifted relative to the others by 10 WFC pixels (1.0'') providing a partial overlap of the chip fields. After pipeline processing, standard IRAF/STSDAS routines were employed to shift and combine the

frames to remove both cosmic rays and hot pixels. Corrections for under-sampling of the point spread function and geometric distortion of the optics were made using the DITHER package within IRAF (Fruchter & Hook 1997). The final frame (Fig. 1) has a pixel scale of 0.05'', an effective resolution of 0.15'' and a  $1\sigma$  detection limit within the seeing disk of  $R_{702} \simeq 31$ .

To produce a catalog of faint arclets from our data we first analysed the *HST* frame using the SExtractor package (Bertin & Arnouts 1996). All objects with isophotal areas in excess of 30 pixels (0.074 arcsec $^2$ ) at the  $\mu_{702} = 24.5$  mag arcsec $^{-2}$  isophote ( $3\sigma$ /pixel) were selected. A steep roll-over in the observed differential number counts arising from incompleteness occurs at  $R_{702} \sim 25.5$ . We estimate the completeness to be  $\sim 80\%$  (approximately  $5\sigma$ ) at  $R_{702} \sim 25.5$ , which we adopt as our magnitude limit, giving a total of 457 sources within a 4.9 arcmin $^2$  area (excluding the PC chip). Seventeen of these sources are classified as star-like on the basis of their profile shapes and are excluded from our analysis.

For the purposes of the photometric analysis presented in Table 1 we correct the F702W photometry ( $R_{702}$ ) to the Cousins *R*-band in the following manner. The observed range in  $(B-R)$  colors of the arcs roughly translates to  $0.2 < (V-R) < 1.0$  giving a typical color of  $(V-R) \sim 0.6$ . Adopting this color we obtain a correction of  $R_{702} - R = 0.2$  (Holtzman et al. 1995), and estimate that this correction introduces a systematic uncertainty in the *R*-band photometry of  $\pm 0.06$  magnitudes.

The final *HST* frame (Fig. 1) reveals many previously unknown strongly lensed features, including a giant arc and two radial arcs, making A 383 a striking new addition to the catalog of cluster lenses at intermediate redshifts.

### 2.2. Ground-based Imaging

With the aim of extending our lensing mass map to the turn-around radius of the cluster, we have used the 3.6m Canada-France-Hawaii Telescope (CFHT) with the CFH12K camera to obtain panoramic images of A 383 on the nights of November 14–16, 1999. Total exposure times of 7.2 ks, 6.0 ks and 3.6 ks, accumulated at 6–10 dither positions, were acquired in the *B*, *R* and *I* bands respectively. Data reduction was performed within IRAF using the MSCRED package including standard bias subtraction and flat-fielding using twilight flats. The dithered exposures were aligned with the Digital Sky Survey frame of the same field to an rms accuracy of 0.15''. More information on the reduction and analysis of these observations will be presented in a forthcoming paper (Czoske et al. 2000). Here we use the central regions of the *B* and *I* band frames to provide photometry of the lensed features in the cluster core (see Table 1). These two frames have seeing of 0.88'' and 0.71'' FWHM respectively.

In addition to the CFH12K imaging, we have obtained *K*-band images of the core of A 383 with the UFTI imager on the 3.8m United Kingdom Infrared Telescope (UKIRT), Mauna Kea, on October 14, 1999. The final frame was accumulated in 27 dithered sub-exposures of 90 s duration each to give a total on-source integration time of 2.4 ks, all in photometric conditions. Employing standard procedures these frames were reduced, combined and calibrated using observations of UKIRT faint standards bracketing the science exposures. The final frame has seeing of 0.42'' FWHM with 0.09''/pixel sampling and an effective  $5\sigma$  depth of  $K = 20.3$ .

Optical and optical-infrared colors of the lensed features in A 383 were measured off the aligned and seeing-matched *BRIK*

fig1.gif

FIG. 1. – The central region of A 383 as observed with *HST* WFPC2, overlaid with an isodensity representation of our lens model. Contours correspond to projected surface mass densities of 3, 4, 6, 8, 11,  $15 \times 10^9 M_{\odot} \text{ kpc}^{-2}$ . The numerical labels indicate the cluster members used in the lens model. The alpha-numeric labels identify the multiple images used to constrain the lens model and a number of other singly-imaged arclets. The spiral galaxy labeled B16 was included in our spectroscopic sample and has  $z = 0.6560$ . The disturbed morphology of the central galaxy, including what appears to be a dust lane passing between two peaks in the light profile, is apparent in the center of this figure.

frames using apertures designed for individual arcs. The arcs were first masked out of the science frame and the sky background estimated by median smoothing over the aperture defined by the absent arc. The sky subtraction was then performed and the individual arc apertures applied to the sky-subtracted frame to obtain the *BRIK* photometry presented in Table 1. Error bars were estimated by varying the smoothing length used in estimating the sky background.

### 2.3. Spectroscopy

On January 26, 2000 we observed the cD galaxy in A 383 with the Wide Field Grism Spectrograph on the University of Hawaii's 2.2-m telescope. The low dispersion spectrum obtained in a 1.8 ks exposure in extremely poor seeing ( $2.7''$ ) shows the full range of emission lines typically found in cD galaxies in cooling flow clusters (e.g. Crawford et al. 1999) and places the cD at a heliocentric redshift of  $z = 0.1880 \pm 0.0012$ .

On January 29, 2000 we obtained 28 additional spectra with the LRIS spectrograph (Oke et al. 1995) on the Keck-II 10-m telescope in MOS mode, with a total exposure time of 3.6 ks in average seeing of  $0.9''$ . Use of the 300/5000 grating centered at 7500 Å provided wide spectral coverage (5000–10,000 Å) at a spectral resolution of 2.55 Å/pixel. Redshifts were measured independently by three members of our team (OC, HE, JPK) and also using the RVSAO cross-correlation package under IRAF to accurately estimate the errors. Successive  $3\sigma$  clipping around the peak of the radial velocity distribution yields a redshift of  $z = 0.1880 \pm 0.0002$  for A 383 and a velocity dispersion of  $\sigma = 1150^{+150}_{-200}$  km s<sup>-1</sup> from 18 galaxy redshifts. Ten other galaxies were found to be background, including B16 at  $z = 0.656$ , which lies close to the cluster core (see Fig. 1).

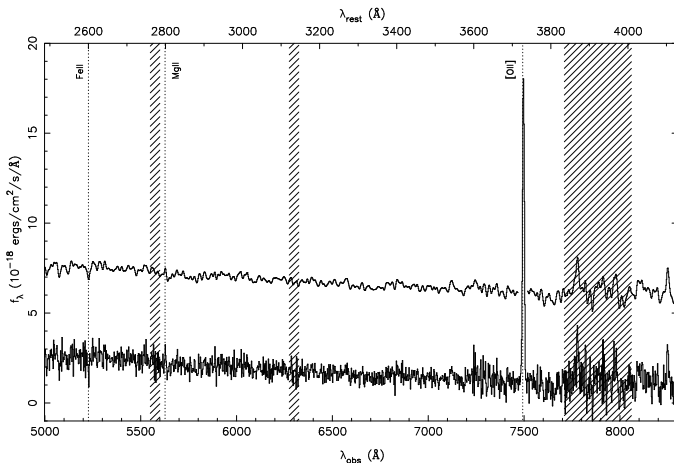


FIG. 2. – The spectrum of arc B0a in A 383 taken with the LRIS spectrograph on the Keck-II 10m telescope. The arc exhibits a blue continuum and we identify the strong emission line as [OII] $\lambda$ 3727 and confirm this with several UV absorption features (marked) to give a redshift of  $z = 1.0103 \pm 0.0001$ . The upper spectrum is smoothed to the nominal resolution of the spectrograph and offset vertically for clarity. The shaded regions show areas of the spectrum strongly affected by night sky lines.

We also obtained a spectrum of the lensed feature B0a which we show in Fig. 2. We identify the strong emission line at 7493 Å as [OII] $\lambda$ 3727 which places the galaxy at a redshift of  $z = 1.0103 \pm 0.0001$ . This interpretation is confirmed by the identification of FeII  $\lambda$ 2600 and MgII  $\lambda$ 2800 absorption features. The properties of this galaxy are discussed further in §3.

### 2.4. ROSAT/HRI Observation

A 383 was observed with the *ROSAT* HRI in February 1995 for a total integration time of 27.4 ks (ROR #800890). An adap-

tively smoothed map of the observed X-ray emission (created using the ASMOOTH algorithm of Ebeling, White & Rangarajan 2000) is shown in Fig. 3. We used a modified version of Steve Snowden's CAST HRI software to correct for exposure time variations across the field of view and subtract a particle background component.

From the fully processed *ROSAT* HRI image the total background-corrected HRI count rate from A 383 is measured to be  $(0.128 \pm 0.005)$  ct s<sup>-1</sup> within 1.5 Mpc ( $6.2'$ ) of the cluster center, using the mean diffuse background at  $r > 2$  Mpc ( $8.2'$ ). Assuming a standard plasma emission spectrum, a Galactic hydrogen column density of  $4.1 \times 10^{20}$  cm<sup>-2</sup> for this sight-line (Dickey & Lockman 1990), a metallicity of 0.3 and an ambient X-ray temperature of  $\sim 7.1$  keV (estimated from the cooling-flow-corrected cluster  $L_X$ - $kT$  relation of Allen & Fabian 1998) we derive a total unabsorbed cluster flux of  $(6.55 \pm 0.23) \times 10^{-12}$  erg cm<sup>-2</sup> s<sup>-1</sup> (0.1–2.4 keV). The corresponding X-ray luminosity is  $(9.8 \pm 0.3) \times 10^{44}$  erg s<sup>-1</sup> (0.1–2.4 keV), in agreement with the XBACs value of  $(8.0 \pm 2.4) \times 10^{44}$  erg s<sup>-1</sup> in the same energy band (Ebeling et al. 1996).

fig3.gif

FIG. 3. – X-ray flux contours of the adaptively smoothed emission from A 383 as seen with the *ROSAT* HRI, overlaid on an *R*-band image of the cluster taken with the CFH12K camera (see §2.2). All X-ray features are at least  $3\sigma$  significant with respect to the local background. The lowest contour lies 30% above the background, adjacent contours differ by 30%. We adjusted the astrometry of the HRI image by  $4''$  (well within the errors of the astrometry solution) to align the X-ray peak with the cD galaxy. The near circular symmetry of the X-ray flux contours reflects the symmetry of the lensing mass contours plotted in Fig. 1. The region shown in our Fig. 1 is marked by the dashed box.

## 3. MODELLING AND RESULTS

In this section we first describe and interpret the multiply-imaged features observed in our *HST* frame of A 383 and explain how these were used to constrain the mass distribution in the central regions of the cluster. We then discuss the form of the mass profile we derive in the very center of the cluster and compare this to theoretical expectations from high resolution N-body simulations. Finally we discuss the X-ray properties of A 383 and compare the mass distribution determined from the lens model with the estimates based on the *ROSAT* data.

### 3.1. Multiply Imaged Features

As a result of the superb resolution of our *HST* images, a detailed analysis of the morphology of the observed arcs allows us to identify seven multiply-imaged systems in the field of A 383. This is significantly greater than the number typically seen in ground-based observations of clusters. We discuss each multiply-imaged system below, and summarize their photometric and spectroscopic properties in Table 1. The lensed features are identified in Fig. 1 and the multiple images are further illustrated below in Fig. 4–6.

### 3.1.1. The Giant and Radial Arcs

We interpret the giant and radial arcs in A 383 as being the lensed images of two background galaxies, B0 and B1, at  $z = 1.01$  (§2.3) and  $z \sim 1.1$  respectively. This interpretation arises from modelling (§3.2) of the radial arcs, which constrains the outer radial arc (B1d) to be a counter image of B1a/b/c at  $z \sim 1.1$ , and the inner radial arc (B0b) to be a counter image of B0a. B0a is also slightly closer to the center of the cluster than other components of the giant arc, supporting the suggestion that it is at a slightly lower redshift than B1.

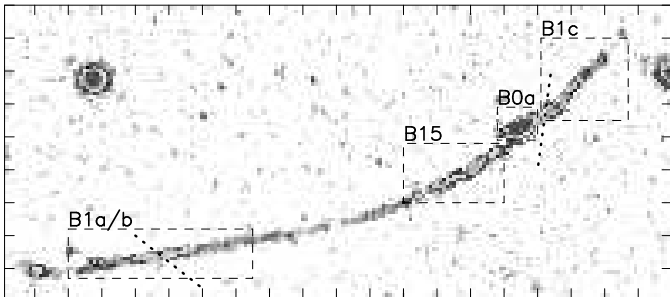


FIG. 4. — The giant arc in A 383 (see text for interpretation). Each tick mark represents  $1''$ , and the orientation is as in Fig. 1. The dotted lines indicate the path of the  $z = 1.1$  critical line close to the observed arcs.

**B0** (Figs. 4 & 5) — This system comprises the brightest component of the giant arc (B0a) and the inner of the two radial arcs (B0b). It is also plausible that B15 is a component of the B0 system given its proximity to B0a in the image plane, however its redder color (Table 1) suggests that it is either singly imaged, or that B0b has a significant color gradient. We are unable to measure the color of B0b to confirm this possibility due to the light from the central galaxy. We have also estimated the unlensed  $R$ -band magnitude of B0 (Table 1) which, along with its blue optical-infrared color, suggests that B0 is a low luminosity star-forming galaxy ( $M_V \sim -19.3$ ).

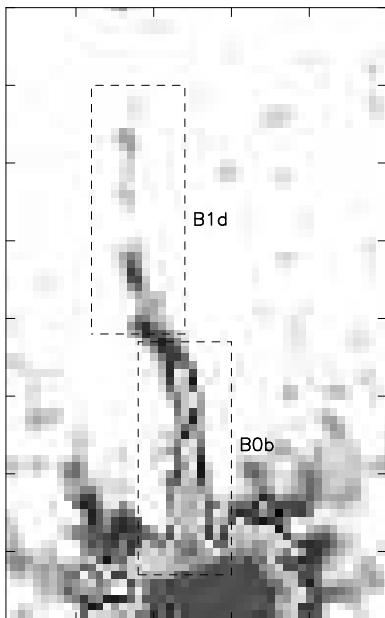


FIG. 5. — A view of the radial arcs as seen on the *HST* frame (enhanced by subtracting a median-smoothed frame from the science frame). Each tick mark represents  $1''$ , and the orientation is as in Fig. 1.

**B1** (Figs. 4 & 5) — B1a/b is a pair of merging images straddling the  $z \sim 1.1$  critical line with counter-images B1c, at the extreme right hand end of the giant arc and B1d, the outer of the

two radial arcs. The lens model (§3.2) and photometric analysis (Table 1) support this interpretation and appear to exclude B15 from being a further counter-image. The unlensed  $R$ -band magnitude of B1 has been estimated (Table 1), from which we determine that it is a very low luminosity galaxy ( $M_V \sim -18.3$ ).

### 3.1.2. Perturbations by Galaxy Halos

**B2 and B3** (Fig. 6) — The lensing effect of neighboring cluster galaxy halos on this complex group of blue arcs demonstrates how galaxy-scale masses measurably perturb the cluster potential. We have modeled the effect of these perturbations and resolved B2 and B3 into two background galaxies, both at a redshift of  $z \sim 3.5$ . Although the photometric analysis is hampered by the nearby galaxy halos, the data presented in Table 1 lend additional support to this interpretation.

B2 comprises five images, of which B2a/b and B2d/e are pairs of images straddling the  $z \sim 3.5$  critical line as it passes around the halos of cluster ellipticals #46 and #23 respectively. B2c lies outside this critical line and has the same parity as B2a. A sixth candidate counter image lies approximately  $1''$  to the left of B3b under the halo of cluster elliptical #23. Multi-band *HST* imaging is necessary to achieve the accurate photometry required to confirm this hypothesis. There is also a low signal-to-noise feature lying in the saddle region between cluster ellipticals #46 and #76, which is probably an extension of B2c. Counter images of this portion of the B2 system are undetected, due to the intrinsic faintness of the galaxy and the relatively low magnification of the counter images relative to the influence of the saddle on the observed feature. Finally, we estimate that the B2 background galaxy has  $M_V \sim -22.0$  and the blue colors typical of a star-forming galaxy.

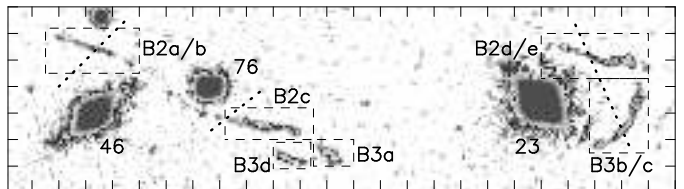


FIG. 6. — The B2/B3 system of arcs (see text for more details). Cluster ellipticals #46, #76 and #23 are also labelled. Each tick mark represents  $1''$ , and the orientation is as in Fig. 1. The dotted lines indicate the path of the  $z = 3.5$  critical line close to the observed arcs.

B3 consists of three images; B3b/c is adjacent to cluster elliptical #23, and B3a, the counter image, lies outside the critical line,  $\sim 1''$  below and to the right of B2c in Fig. 6. B3d appears to be a singly-imaged component of the background galaxy that produces B3a/b/c. This interpretation is supported by the photometric analysis in Table 1. We also estimate that B3 is a star forming galaxy with a similar luminosity ( $M_V \sim -22.4$ ) to B2.

**B4** (Fig. 1) — This is another complex and unusual arc, the precise nature of which is uncertain. One possibility is that B4 is part of a multiple image system containing B6; however, photometric analysis (Table 1) does not support this hypothesis. More complete color information will improve our ability to comment on this arc. If B4 is a singly imaged source it lies at a redshift of  $z \lesssim 1.0$ .

### 3.1.3. Faint Arcs

**B5** (Fig. 1) — B5 is a very faint arc lying in the saddle region between the central galaxy and cluster elliptical #99. We interpret this arc as an image of a background galaxy which is magnified by this saddle and therefore constrain the redshift of the galaxy to be  $z \gtrsim 2.4$ .

*B9a & B9b (Fig. 1)* — This is a pair of extremely faint arcs detected only because of the superb resolution and low sky background of the *HST* observations. Both arcs appear to comprise three images resulting from the magnifying effect of the saddle potential between the cluster center and cluster elliptical #260. We estimate that they lie at a redshift of  $z \gtrsim 3$ .

*B14 (Fig. 1)* — B14 is barely detected above the sky background in the *HST* frame, however we detect it at  $K = 19.70 \pm 0.05$  in the UKIRT frame, giving  $(R-K) = 6.02 \pm 0.11$ . As B14 is singly-imaged, we obtain a redshift limit of  $z \lesssim 3.9$  from our lens model. A full analysis of galaxies exhibiting extreme colors and the general background population lying behind our cluster sample will be presented in a future paper.

### 3.1.4. Arclets

We also detect numerous singly-imaged arclets in the field of A 383 (Fig. 1 and Table 1) and have obtained upper limits on the redshifts of three of these arclets (B6, B7 and B8) on the basis of their singly-imaged nature.

*B6 (Fig. 1)* — We obtain a redshift limit of  $z \lesssim 0.9$  for this arclet, however its blue ( $B-R$ ) and ( $R-I$ ) colors (Table 1) are consistent with it being a star forming galaxy at  $z \sim 1.5-2.0$ . The latter interpretation supports the possibility that B6 and B4 contain multiply imaged features of a single background galaxy. As noted in §3.1.2, improved photometry of B4 will help to resolve this uncertainty.

*B7 (Fig. 1)* — B7 lies at a redshift of  $z \lesssim 1.3$  which, on the basis of its ( $B-R$ ) color (Table 1) is consistent with B7 being a moderately star forming galaxy.

*B8 (Fig. 1)* — This arclet has a redshift limit of  $z \lesssim 2.0$ , while its colors are broadly consistent with this being a star forming galaxy at  $z \sim 1.0-1.4$ .

## 3.2. Lens Model

The mass distribution of A 383 was reconstructed using the parametric lens inversion method described in detail by K96. In addition to a cluster-size mass component, the model contains 29 individual galaxy masses (including the central galaxy) covering the entire *HST* field of view. The parameters describing the model were constrained within the cluster core using four of the multiple image systems identified in the *HST* frame (B0, B1, B2 and B3) and on larger scales using the weak shear field estimated from the shapes of the faint galaxies across the whole frame. The cluster scale mass that dominates the mass distribution has a core radius of  $(46 \pm 3)$  kpc, velocity dispersion of  $(900 \pm 20)$  km s<sup>-1</sup> and a cut-off radius of  $(1200 \pm 100)$  kpc (see K96 for details of how these quantities are defined).

The mass distribution obtained from the lens model is overlaid on the optical image in Fig. 1. We calculate the total projected mass within the radius of the giant arc (65 kpc) to be  $(3.5 \pm 0.1) \times 10^{13} M_{\odot}$ . Using the weak shear measurements we can extend our model to larger scales and constrain the projected mass within a 250 kpc radius of the cluster center to be:  $(1.8 \pm 0.2) \times 10^{14} M_{\odot}$ .

In Fig. 7 we plot the projected surface mass density derived from the lens model as a function of the distance from the cluster center ( $r$ ). On scales  $r \gtrsim 10$  kpc, the density profile is dominated by the cluster-scale potential, the core radius of the cluster-scale mass distribution ( $\sim 46$  kpc) being consistent with previous estimates of core radii from lensing studies (Mellier et al. 1993; Smail et al. 1996; Natarajan et al. 1998). The shape of A 383's profile is however only constrained out to  $r \sim 400$  kpc,

this being the extent of the *WFPC2* field of view. The mass profile is most accurately measured within  $r \sim 100$  kpc where information from the multiple images is available.

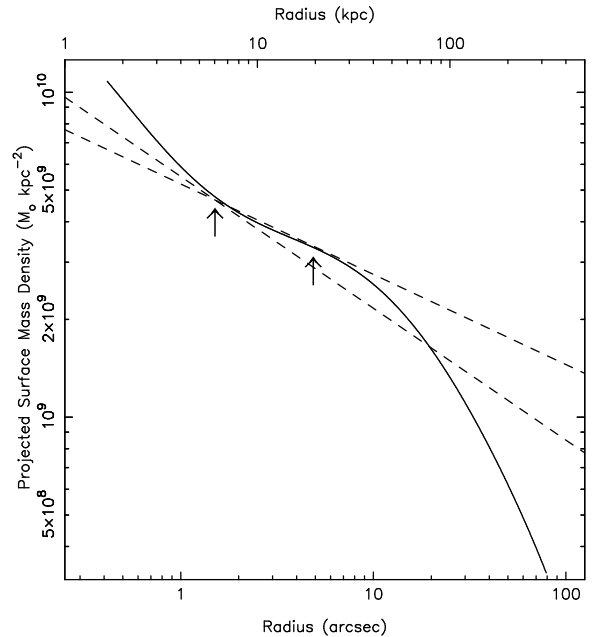


FIG. 7. — The projected surface mass density ( $\Sigma$ ) of A 383 as a function of radius, obtained from the lens model by measuring the mass density in concentric annuli. The dashed lines illustrate the difference between the profile slope at the positions of the two radial arcs (B0b and B1d), which are marked by arrows at 6.0 and 19.9 kpc respectively.

### 3.2.1. Radial Arc Properties

B0b and B1d (see Figs. 1 & 5) lie at distances of  $(6.0 \pm 0.4)$  kpc and  $(19.9 \pm 0.4)$  kpc from the cluster center respectively. These two arcs therefore enable us to probe the shape of the mass distribution on scales of  $r \lesssim 20$  kpc. Specifically, the radial arcs constrain the slope of the density profile, as their radial positions depend on the local gradient of the projected mass, rather than on the mean enclosed surface density.

A detailed analysis of the shape of A 383's density profile is currently limited by the pseudo-isothermal elliptical functional form adopted in the lens model (see K96). However, in order to estimate the slope of the density profile at the positions of the two radial arcs, we fitted various polynomial functions to the density profile data. De-projecting this analysis to obtain the slope of the three-dimensional density profile ( $\rho$ ), we obtain the gradients:  $d(\log \rho)/d(\log r) = -1.41$  and  $-1.29$  at  $r = 6.0$  kpc (B0b) and  $r = 19.9$  kpc (B1d) respectively; the error on these slopes is of the order  $\lesssim 0.03$ .

We interpret this difference in slope at the positions of the two radial arcs, specifically the steeper slope at  $r \sim 6$  kpc, as being due to the presence of a distinct central galaxy halo within the overall cluster halo.

Williams et al. (1999) suggest that radial arcs are a useful test of the lensing role of such central galaxy halos within an overall cluster-scale NFW halo. They predict that  $\log(\theta_r/\theta_t)$  (where  $\theta_r$  and  $\theta_t$  are the angular positions of the radial and tangential arcs respectively) should decrease with decreasing cluster mass as the lensing role of the central galaxy becomes more significant relative to the overall cluster mass distribution. From their Fig. 7 we estimate that for A 383:  $\log(\theta_r/\theta_t) = -0.35$  to  $-0.65$ , taking into account the velocity dispersions obtained from spectroscopy (§2.3) and the lens model (§3.2).

TABLE 1  
Photometry and Spectroscopy of Lensed Features in A 383

Feature	$R$	$(B-R)$	$(R-I)$	$(I-K)$	$z$	$R_{\text{source}}^d$
B0a	$21.98 \pm 0.01$	$1.02 \pm 0.01$	$0.74 \pm 0.01$	$1.91 \pm 0.03$	$1.0103 \pm 0.0001^a$	$25.0 \pm 0.3$
B0b	$21.95 \pm 0.24$	...	...	...		
B1a/b	$21.50 \pm 0.02$	$1.14 \pm 0.03$	$1.07 \pm 0.04$	$2.06 \pm 0.14$	$1.1 \pm 0.1$	$26.7 \pm 0.6$
B1c	$23.03 \pm 0.02$	$1.11 \pm 0.03$	$1.00 \pm 0.03$	$1.90 \pm 0.07$		
B1d	$23.94 \pm 0.07$	...	...	...		
B2a/b	$23.79 \pm 0.06$	...	...	...	$3.5 \pm 0.2$	$26.8 \pm 0.7$
B2c	$23.90 \pm 0.01$	$0.87 \pm 0.03$	$0.29 \pm 0.02$	$1.94 \pm 0.08$		
B2d/e	$22.56 \pm 0.21$	$0.75 \pm 0.26$	$0.54 \pm 0.23$	$< 2.3$		
B3a	$23.80 \pm 0.02$	$0.83 \pm 0.02$	$0.40 \pm 0.02$	$< 1.9$	$3.5 \pm 0.2$	$26.3 \pm 0.2$
B3b/c	$22.62 \pm 0.24$	$0.66 \pm 0.27$	$0.59 \pm 0.27$	$< 2.5$		
B3d	$23.86 \pm 0.02$	$1.09 \pm 0.03$	$0.50 \pm 0.02$	$< 2.0$		
B4	$22.07 \pm 0.01$	$0.94 \pm 0.26$	$< 0.4$	...	$\approx 1.0^b$	...
B5	$23.35 \pm 0.03$	...	...	...	$\approx 2.4$	...
B6	$23.42 \pm 0.01$	$0.42 \pm 0.03$	$0.12 \pm 0.07$	$< 3.5$	$\approx 0.9^b$	...
B7	$24.23 \pm 0.02$	$0.63 \pm 0.02$	$< 0.5$	...	$\approx 1.3^b$	...
B8	$24.68 \pm 0.05$	$0.84 \pm 0.14$	$0.81 \pm 0.17$	$< 4.1$	$\approx 2.0^b$	...
B9a	$25.20 \pm 0.11$	...	...	...	$> 3.0$	...
B9b	$24.48 \pm 0.08$	...	...	...	$> 3.0$	...
B10	$24.85 \pm 0.05$	$0.19 \pm 0.03$	$0.57 \pm 0.07$	$< 4.5$	...	...
B11	$22.92 \pm 0.01$	$1.60 \pm 0.01$	$1.02 \pm 0.01$	$2.46 \pm 0.01$	...	...
B12	$23.56 \pm 0.02$	...	...	...	...	...
B13	$23.97 \pm 0.01$	$1.45 \pm 0.14$	$1.05 \pm 0.16$	$2.19 \pm 0.18$	...	...
B14 <sup>c</sup>	$26.12 \pm 0.02$	$> 1.2$	$< 2.0$	$> 4.0$	$\approx 3.9$	...
B15	$22.23 \pm 0.02$	$1.35 \pm 0.01$	$0.94 \pm 0.02$	$1.96 \pm 0.09$	$1.1 \pm 0.1$	...
$L_*$ Cluster E/S0	18.01	2.44	0.67	2.50	0.188	

a) Spectroscopic redshift; b) Redshift assumes single image; c) Extremely Red Object with  $(R-K) = 6.02 \pm 0.11$ . d) Estimated  $R$ -band magnitude of the background galaxy, corrected for lens amplification; the error bars reflect the uncertainties in the lens model and generally scale with the number of multiple images per background galaxy.

We have computed angular position ratios of  $\log(\theta_r/\theta_t) = -1.04 \pm 0.07$  and  $-0.51 \pm 0.03$  for A 383's inner (B0b) and outer (B1d) radial arcs respectively. The outer radial arc appears to be consistent with Williams et al.'s predictions, however the inner radial arc falls well outside their prediction. This discrepancy may be due to simplifying assumptions made by Williams et al. regarding the nature and complexity of cluster substructure. We also note that, due to the (almost) circular symmetry of A 383, the radial arcs are not forced to lie at the radial critical line in the image plane. This is another potential source of discrepancy between the observations and the predictions.

### 3.2.2. Comparison With Numerical Simulations

Ghigna et al. (2000) have performed numerical simulations of galaxy clusters at the highest resolution to date, resolving structure down to scales of  $r \sim 5$  kpc. They find a de-projected slope of  $-1.6 \pm 0.1$  on scales of  $r = 5-100$  kpc in a  $\sigma \sim 800 \text{ km s}^{-1}$  cluster. This is steeper than the density profile of A 383 on comparable scales,  $\sim -1.3$  (see §3.2.1 and Fig. 7). We will present a detailed comparison of the lens model using NFW and Moore et al. (1998) density profiles in a subsequent paper.

Recent progress has also been made in the inclusion of gas in numerical simulations (e.g. Pearce et al. 1999). However, the resolution of these simulations precludes analysis of the form of the mass profile on the scales probed by the radial arcs in A 383 ( $r \lesssim 20$  pc). Higher resolution simulations including gas cooling have been performed by Lewis et al. (1999). However, these authors concede that the mass of the central galaxies in their simulations is unrealistically high, which hampers a reli-

able comparison with our observations of A 383.

The constraints on the density profile derived from the radial arcs in A 383 confirm the need for a massive central galaxy to explain the lensing properties of this X-ray luminous cluster. Our observations therefore support the case for increasing the resolution of N-body simulations of clusters including gas physics.

### 3.3. X-ray Properties of A 383

The radial X-ray surface brightness profile around the cluster X-ray centroid is shown in Fig. 8. We attempt to describe the X-ray emission profile by fitting a standard beta model (Cavaliere & Fusco-Femiano 1978)

$$I(s) = I_0 \left(1 + \left(\frac{r}{r_c^{3d}}\right)^2\right)^{-3\beta+0.5},$$

convolved with the *HRI* point-spread function (PSF), to the observed X-ray surface brightness distribution. The free fit parameters are the peak surface brightness ( $I_0$ ), the 3-d core radius ( $r_c^{3d}$ ), and the slope parameter ( $\beta$ ). We note that the use of the beta model implies that the gas is isothermal and in hydrostatic equilibrium. While these assumptions are likely to be violated in most clusters, numerical simulations show that using the beta model introduces, on average, no bias and only a moderate scatter of typically 20% in the cluster mass estimates (Evrard, Metzler & Navarro 1996).

We fit two beta models, one to the full radial range of the data including the likely cooling flow region (model A), and a second one to the outer regions only (model B). While model A yields a poor description of the X-ray emission at large radii

(see Fig. 8) it provides us with an acceptable fit to, and an analytic description of, the emission profile at  $r \lesssim 100$  kpc, which can be used to derive the gas density and, assuming hydrostatic equilibrium, the total binding mass within the core region (see below). Model B, obtained by fitting only the range from  $r = 12$  kpc to 850 kpc ( $3.5'$ ), describes the non-cooling-flow component (Fig. 8), for which we find  $r_c^{3d} = (23 \pm 3)''$ , corresponding to  $(93 \pm 12)$  kpc, and  $\beta = 0.65 \pm 0.03$ , consistent with the canonical value of  $2/3$ . The quoted errors include systematic uncertainties which we explored by varying the radial range used for the fit.

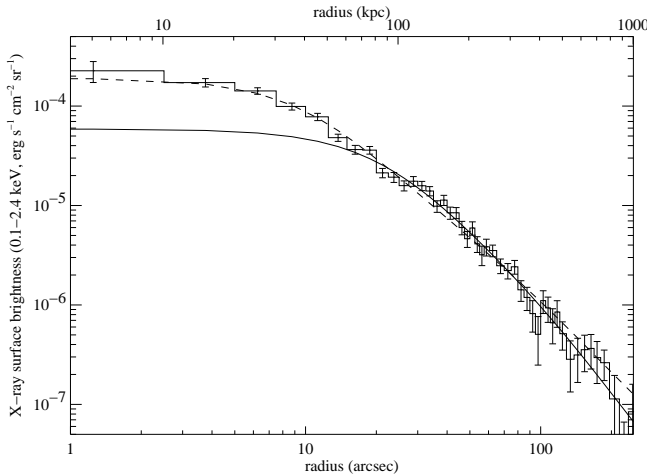


FIG. 8. – The radial X-ray surface brightness profile of A 383 as observed with the *ROSAT HRI*. Overlaid are the best-fit beta models (convolved with the *HRI* PSF) and fitted to the full profile (model A, dashed line) or to the outer regions only (model B, solid line). The excess emission in the cluster core is caused by an additional cooling flow component, which is not included in the models.

Subtracting beta model B from the observed profile we find the cooling flow to contribute 13% to the total cluster flux within a radius of 500 kpc, corresponding to a luminosity of  $1 \times 10^{44}$  erg s $^{-1}$  (0.1–2.4 keV). A rough (usually low) estimate of the mass deposition rate,  $\dot{M}$ , can be obtained by converting this excess luminosity to the bolometric band (by multiplying by a factor of 3.03 appropriate for the assumed cluster gas temperature of 7.1 keV) and equating it to the luminosity of the cooling flow

$$L_{\text{cool}} = \frac{5}{2} \frac{\dot{M}}{\mu m_p} kT$$

(Fabian 1994). We thus derive a lower limit to the mass deposition rate of  $\dot{M} \gtrsim 200 M_{\odot} \text{ yr}^{-1}$ , a value typical of moderate cooling-flow clusters (e.g. Peres et al. 1998).

Under the assumption of hydrostatic equilibrium, and using a beta model to describe the radial gas density profile, the total gravitational mass within a projected radius  $r$  can be derived from

$$M(< r) = \frac{3\beta kT r_c^{3d}}{\mu m_p G} \frac{\pi}{2} \frac{(r/r_c^{3d})^2}{\sqrt{1+(r/r_c^{3d})^2}}$$

(Soucail et al. 2000).

Using the parameters of model A we estimate the projected mass within a radius of 65 kpc to be  $4.0_{-1.7}^{+1.1} \times 10^{13} M_{\odot}$ , in good agreement with our lensing mass measurement of  $(3.5 \pm 0.1) \times 10^{13} M_{\odot}$  within the same projected radius (§3.2). The equivalent mass estimate within a radius of 250 kpc is more uncertain, but is approximately  $(1.2 \pm 0.5) \times 10^{14} M_{\odot}$ , again in reasonable agreement with the lensing measurement. We note that the bulk of the uncertainty in the X-ray mass estimates is caused by the adopted error of  $\pm 2$  keV in the global gas temperature,

$kT$ . Forthcoming observations of our full cluster sample with *Newton* will allow us to obtain much more accurate X-ray mass measurements on scales of  $\sim 10$ –1000 kpc.

#### 4. DISCUSSION AND CONCLUSIONS

We have discovered numerous new gravitationally lensed features, including a giant arc and two radial arcs in A 383, a massive, X-ray luminous cluster of galaxies at a redshift of  $z = 0.188$ . This is the first cluster in which two radial arcs have been identified and these provide a detailed view of the cluster mass distribution on scales of  $r \lesssim 20$  kpc.

The morphologies and positions of the arcs have been used, in conjunction with ground-based multi-color photometry, to constrain the mass distribution and compute a precise mass density profile of this cluster within a radius of  $\sim 250$  kpc.

Within the core radius ( $r = 46 \pm 3$  kpc) derived from the lensing analysis, the density profile exhibits a shallower slope ( $d(\log \rho)/d(\log r) = -1.29 \pm 0.03$ ) than a Moore profile (Moore et al. 1998; Ghigna et al. 2000) and a steeper slope than a single NFW profile.

We have also analysed the properties of the two radial arcs, interpreting the difference in angular position of these arcs as a signature of the lensing role of the massive central galaxy. This supports the proposal by Williams et al. (1999) that massive central galaxy halos are required to explain the lensing properties of the cores of massive clusters ( $\sigma \sim 1000$  km s $^{-1}$ ). However, only the outer radial arc of A 383 falls within the range predicted by Williams et al. for the angular position ratio of radial and tangential arcs. The inner radial arc lies well outside of their predicted range. This discrepancy is probably caused by simplifying assumptions in Williams et al.’s theoretical models.

The lensing analysis is complemented by an analysis of the cluster’s X-ray properties as obtained from archival *ROSAT HRI* data. We find strong evidence for a cooling flow in agreement with the optical properties of the cluster, and derive a lower limit on the mass deposition rate of  $200 M_{\odot} \text{ yr}^{-1}$ , typical of moderate cooling flow clusters. The X-ray estimates for the total mass within the projected radius of the giant arc are in good agreement with the lensing measurements and are consistent with earlier claims (e.g. Allen 1998) that significant discrepancies between lensing and X-ray mass estimates are caused by substructure in unrelaxed, non-cooling-flow systems.

We note that the cluster sample used in our survey is effectively X-ray selected, thus allowing us, for the first time, to measure in detail the mass distribution in massive clusters of galaxies unaffected by selection biases. The theme of our future program will be to analyse the lensing signal and X-ray emission (as observed with *Newton*) from all twelve clusters in our sample and to trace the form of the mass profile from 50 kpc to 5 Mpc. We will investigate the dispersion in the profiles and the core properties of the clusters and determine how these correlate with the cluster’s dynamical state and the presence of a cooling flow. We shall also attempt to constrain the high end of the cluster mass function and calibrate directly the cluster mass-temperature and mass-luminosity relations at  $z \sim 0.2$ .

#### ACKNOWLEDGEMENTS

We thank John Blakeslee, Alastair Edge, Ben Moore, Frazer Pearce and Liliya Williams for helpful conversations and assistance. Thanks also go to Laurence Jones for helping with the Keck/MOS observations.

GPS acknowledges support from PPARC. JPK acknowl-

edges support from CNRS. HE gratefully acknowledges financial support by NASA LTSA grant NAG 5-8253. OC acknowledges support from the European Commission under contract no. ER-BFM-BI-CT97-2471. IRS acknowledges support from a Royal Society University Research Fellowship. We also acknowledge financial support from the UK-French AL-

LIANCE collaboration programme #00161XM.

UKIRT is operated by the Joint Astronomy Centre on behalf of the Particle Physics and Astronomy Research Council of the United Kingdom. The W. M. Keck Observatory is operated as a scientific partnership among the California Institute of Technology, the University of California and NASA.

## REFERENCES

- Allen, S.W., 1998, MNRAS, 296, 392  
 Allen, S.W., Fabian, A.C., 1998, MNRAS, 297, 57  
 Abell, G.O., Corwin, H.G., Jr., Olowin, R.P., 1989, ApJS, 70, 1  
 Bahcall, N.A., Fan, X., Cen, R., 1997, ApJ, 485, L53  
 Bertin, E., Arnouts, S., 1996, A&A, 117, 393  
 Cavaliere, A., Fusco-Femiano, R., 1978, A&A, 49, 137  
 Crawford, C.S., Allen, S.W., Ebeling, H., Edge, A.C., Fabian, A.C., 1999, MNRAS, 306, 857  
 Czoske, O., et al., 2000, in preparation  
 DeGrandi, S. et al., 1999, ApJ, 514, 148  
 Dickey, J.M., Lockman, F.J., 1990, ARA&A, 28, 215  
 Ebeling, H., et al., 1996, MNRAS, 281, 799  
 Ebeling, H., et al., 1998, MNRAS, 301, 881  
 Ebeling, H., et al., 2000, MNRAS, in press  
 Ebeling, H., Edge, A.C., Henry J.P., 2000, in Large Scale Structure in the X-ray Universe, Proceedings of the 20-22 September 1999 Workshop, Santorini, Greece, eds. Plionis, M., Georgantopoulos, I., Atlantisciences, Paris, France, p.39  
 Eke, V.R., Cole, S., Frenk, C.S., 1996, MNRAS, 282, 263  
 Evrard, A.E., Metzler, C.A., Navarro, J.F., 1996, ApJ, 469, 494  
 Fabian, A.C., 1994, AR&A, 32, 277  
 Fahlman, G., Kaiser, N., Squires, G., Woods, D., 1994, ApJ, 437, 56  
 Fort, B., Le Fèvre, O., Hammer F., Cailloux, M., 1992, ApJ, 399, L125  
 Fruchter, A.S., Hook, R.N., 1997, in Applications of Digital Image Processing, Proc. SPIE, 3164, ed. Tescher, A., p120  
 Ghigna, S., Moore, B., Governato, F., Lake, G., Quinn, T., Stadel, J., 2000, ApJ, in press  
 Gioia I.M., et al. 1990, ApJL, 356, 35  
 Holtzman, J.A., Burrows, C.J., Casertano, S., Hester, J.J., Trauger, J.T., Watson, A.M., Worthey, G., 1995, PASP, 107, 1065  
 Kay, S.T., Bower, R.G., 1999, MNRAS, 308, 664  
 Kneib, J.-P., Mellier, Y., Fort, B., Soucail, G., Longaretti, P.Y., 1994, A&A, 286, 701  
 Kneib, J.-P., Ellis, R.S., Smail, I., Couch, W.J., Sharples, R.M., 1996, ApJ, 471, 643  
 Lewis, G.F., Babul, A., Katz, N., Quinn, T., Hernquist, L., Weinberg, D.H., 1999, astro-ph/9907097  
 Mellier, Y., Fort, B., Kneib J.-P., 1993, ApJ, 407, 33  
 Moore, B., Governato, F., Quinn, T., Stadel, J., Lake, G., 1998 ApJL, 499, 5  
 Natarajan, P., Kneib, J.-P., Smail, I., Ellis, R.S., 1998, ApJ, 499, 600  
 Navarro, J.F., Frenk, C.S., White, S.D.M., 1997, ApJ, 490, 493  
 Oke, J.B., et al., 1995, PASP, 107, 375  
 Pearce, F.R., Thomas, P.A., Couchman, H.M.P., Edge, A.C., 2000, MNRAS, in press  
 Peres, C.B., Fabian, A.C., Edge, A.C., Allen, S.W., Johnstone, R.M., White, D.A., 1998, MNRAS, 298, 416  
 Smail, I., Couch, W.J., Ellis, R.S., Sharples, R.M., 1995, ApJ, 440, 501  
 Smail, I., et al., 1996, ApJ, 469, 508  
 Smail, I., Ellis, R.S., Dressler, A., Couch, W.J., Oemler, A., Butcher, H., Sharples, R.M., 1997, ApJ, 470, 70  
 Soucail G., Ota, N., Boehringer, H., Czoske, O., Hattori, M., Mellier, Y., 2000, A&A, 355, 433  
 Tyson, J.A., Wenk, R.A., Valdes, F., 1990, ApJ, 349, 1  
 Williams, L.L.R., Navarro, J.F., Bartelmann, M., 1999, ApJ, 527, 535  
 Viana, P.T.P., Liddle, A.R., 1996, MNRAS, 281, 323

This figure "fig1.gif" is available in "gif" format from:

<http://arxiv.org/ps/astro-ph/0008315v1>

This figure "fig3.gif" is available in "gif" format from:

<http://arxiv.org/ps/astro-ph/0008315v1>